Available online at www.sciencedirect.com
ScienceDirect
Trans. Nonferrous Met. Soc. China 35(2025) 1837−1854
Transactions of Nonferrous Metals Society of China
www.tnmsc.cn

Synthesis and interfacial characterization of Cr/CoNiCrAlTaY bilayer coating on γ-TiAl alloy for oxidation protection

Zhen ZENG[1], Yong-sheng WANG[1], Ya-rong WANG[1], Bing ZHOU[1], Ke ZHENG[1],
Wan-yuan GUI[2], Yan-li WANG[3], Sheng-wang YU[1], Jun-pin LIN[3]

1. College of Materials Science and Engineering, Taiyuan University of Technology, Taiyuan 030024, China;
2. National Center for Materials Service Safety, University of Science and Technology Beijing, Beijing 100083, China;
3. State Key Laboratory for Advanced Metals and Materials, University of Science and Technology Beijing, Beijing 100083, China

Received 16 October 2023; accepted 19 July 2024

Abstract: A Cr/CoNiCrAlTaY bilayer coating was prepared on the Ti−45Al−8.5Nb alloy by plasma surface metallurgy technique. The as-prepared coating with a grain size of ~2 μm exhibited a dense microstructure and strong adhesion due to metallurgical bonding, consisting of outermost Cr layer and CoNiCrAlTaY transition layer. The typical power-law relationship between mass gain and time was obtained for the coated specimens with a rate exponent of 3.18 following oxidation at 1173 K. The top Cr_2O_3 film and spinel oxides (i.e., $NiCr_2O_4$ and $CoCr_2O_4$) exhibited a protective effect with a low oxidation reaction rate. Interfacial analysis identified Ta precipitates (Cr_2Ta and $TaAl_3$) and Ta oxides (Ta_2O_5 and Ta_2O_3), which played an essential role in retarding rapid diffusion and enhancing adhesion and oxidation resistance.

Key words: TiAl alloy; Cr/CoNiCrAlTaY coating; oxidation resistance; interface; adhesion

---

1 Introduction

γ-TiAl alloy has a broad application in the aerospace industry due to the superior properties such as low density, high specific strength, and good creep resistance at high temperatures [1−3]. However, the similar oxygenophilic elements Ti and Al in γ-TiAl alloy can promote the formation of mixed TiO_2 and Al_2O_3 instead of a protective α-Al_2O_3 film in the range of 1023−1073 K, which deteriorates the oxidation resistance [2−4]. MCrAlY (M=Ni and/or Co) coatings as a typical bonding layer of thermal barrier coatings (TBCs) have been successfully applied to Ni-based superalloys [5]. Inspired by this design, MCrAlY coatings have been prepared on γ-TiAl alloy [5−7], achieving the improved oxidation resistance of TiAl alloys by forming a continuous Al_2O_3 scale. However, applying these coatings on TiAl alloys remains limited by degradation caused by the interfacial interdiffusion of elements, i.e., compositionally rich/poor layers, where thermally grown oxide could induce thermal stress and microcracks.

To alleviate these issues, several strategies have been extensively proposed, including diffusion barriers (i.e., Al_2O_3 [8,9], Cr_2O_3 [10], Cr, and Mo [11,12]) between the coating and TiAl alloy, or doping refractory metals (i.e., Ru, Hf, Re, and Ta [13−15]) in MCrAlY (M=Ni and/or Co) coatings. In the diffusion barrier, new issues are inevitable at the interface of the MCrAlY coatings/diffusion barrier/TiAl alloys due to mismatch in physical and mechanical properties (i.e., coefficient of thermal

---

Corresponding author: Yong-sheng WANG, Tel: +86-18636869409, E-mail: wangyongsheng@tyut.edu.cn

https://doi.org/10.1016/S1003-6326(25)66786-0

expansion and Young's modulus) during thermal cycling [8]. Alternatively, refractory metal-doped MCrAlY coatings exhibit a stable microstructure and sluggish interdiffusion, indicating promising research significance. The refractory element Ta serves as a stabilizer for Ti and Nb metals, suppressing degradation of the microstructure and mechanical properties of TiAl alloys [16,17]. Moreover, Ta-doped MCrAlY coatings have shown good properties in retarding the interdiffusion [18]. However, several factors including the preparation method, Ta content, and phase/structure will play the combined roles in the performance of Ta-doped MCrAlY coatings, leading to controversial results [19,20]. Moreover, the various mobilities of atoms can lead to transformation among multi-phases, along with the generation of oxides during high-temperature oxidation under practical oxygen pressure. Thus, the roles of phase transition and the oxide/alloy interface during the oxidation remain unclear. Furthermore, due to a trace amount of refractory elements (1%−10% of Ta addition), the Ta microstructures in the coatings remain unknown, limiting the further understanding of microstructure and oxide evolution during oxidation. Therefore, it is important to study the phase evolution of Ta-doped MCrAlY coatings and interfacial structure during oxidation at high temperature.

Plasma surface metallurgy technique (PSMT) offers significant advantages, including metallurgical bonding between the coating/substrate, gradient distribution of the elements, and no pollution [21]. Coatings prepared by PSMT exhibit fine grains, good crystallinity, high orientation randomness, and a dense structure, differing from coatings prepared by high-velocity oxygen fuel (HVOF) [22−24]. This approach has also been used to improve the surface properties (e.g., hardness, wear, corrosion, and oxidation resistance) of various substrates, such as Mo [25], Cr [26], and CrCoNiAlTiY [27] coating on γ-TiAl alloy and NiCoCrAlY coating on Inconel 718 alloy [28,29]. A robust coating of aerospace components (e.g., turbine blades) requires certain characteristics including a stable microstructure, good oxidation resistance, strong adhesion, and spallation resistance to ensure its stability in the service environment. Cr_2O_3, formed from pure Cr or Cr alloys at high temperature, will grow slowly, and it has been extensively utilized as an oxygen barrier and corrosion-resistant material. This work has studied the deposition of Cr/CoCrNiAlTaY bilayer coatings onto γ-TiAl alloy using PSMT, to achieve coatings with enhanced adhesion and oxidation resistance. In this study, the growth behavior of thermally growth oxides (TGO) during high-temperature oxidation was investigated by X-ray diffraction (XRD) and scanning electron microscopy (SEM). Furthermore, transmission electron microscopy (TEM) was used to examine the transformation of Ta precipitates and interfaces after oxidation, offering further insights into the influence of Ta doping on the oxidation resistance of MCrAlY coatings.

2 Experimental

2.1 Substrate materials

An ingot with a nominal chemical composition of Ti−45Al−8.5Nb−0.2W−0.2B−0.02Y (atomic ratio), abbreviated as Ti−45Al−8.5Nb alloy, was prepared by magnetic levitation melting. Specimens with dimensions of 10 mm × 10 mm × 5 mm were cut by wire electrical discharge machining as substrate. Before fabricating the coatings, all specimens were ground and polished to a mirror-like surface, ultrasonically cleaned in alcohol for 5 min, and then dried with an air drier.

2.2 Coating preparation

PSMT was used to deposit coatings on Ti−45Al−8.5Nb specimens. The plate target with a chemical composition of Co−30Ni−20Cr−12Al−2Ta−0.2Y (wt.%) served as the transition layer. A Cr target with 99.95% purity was used as the external coating to deposit Cr/CoNiCrAlTaY bilayer on the substrate. The CoNiCrAlTaY target was prepared by powder metallurgy [21,27−29]. The deposition process was conducted at 1123 K in a high-purity Ar atmosphere (~99.99% purity) for 30 min. The working pressure was set as 4×10^{-2} Pa, and argon gas was pressurized to 44 Pa. The source and cathode voltages were set as 700 and 445 V, respectively. All surfaces of each substrate were coated with the Cr/CoNiCrAlTaY bilayer coating to avoid mass measurement errors caused by uncovered surfaces during oxidation.

2.3 Oxidation and characterization

The initial size and mass of each sample were measured, and the samples were placed in quartz crucibles. The samples and quartzes crucible were weighed using an electrical balance with an accuracy of 0.0001 g (ME104E), and then placed together in a corundum crucible for oxidation at 1173 K in a muffle furnace. The crucibles and samples were removed and cooled to room temperature after 10 h of oxidation. The total mass including the crucibles and samples (and spalling parts) was measured by an analytical balance at least five times. Then, the samples and quartz crucibles were put back in the muffle furnace.

The surface morphologies of Cr/CoNiCrAlTaY coated specimens were analyzed before and after oxidation by SEM (Zeiss Gemini300, Germany), and the chemical composition was analyzed by energy-dispersive X-ray spectroscopy (EDS). The microstructure of the samples was examined by XRD (Rigaku DX−2700, Cu K_α radiation, Japan) at a step angle of 0.01° and a scanning speed of 10 (°)/min. The microstructure of oxides and chemical analysis were studied by a transmission electron microscope (TEM, FEI-Talos F200S/FEI Tecnai G2 F20 X-Twin, USA) equipped with EDS. The specimens for TEM testing were prepared by using a focused ion beam (FIB, FEI NanoLab Strata 400S, USA). The scratch test was carried out by a scratch tester (HT−3001A) to obtain the adhesion the oxide scale/film/Ti−45Al−8.5Nb substrate. A scratch tester with a Rockwell diamond indenter applied a load increasing at 80 N/min up to 200 N.

3 Results

3.1 Microstructure of as-prepared Cr/CoNiCrAlTaY coating

Figure 1 shows the XRD pattern of the as-prepared Cr/CoNiCrAlTaY coating, where the diffraction peaks at 38.1°, 40.2° and 43.5° are assigned to the outermost Cr coating. Comparison with PDF standards reveals the presence of several compounds (i.e., $AlCr_2$, Co_2Ta, Al_3Ni_2, $TaAl_3$ and AlCo), suggesting that the CoNiCrAlTaY transition layer comprises multiple phases.

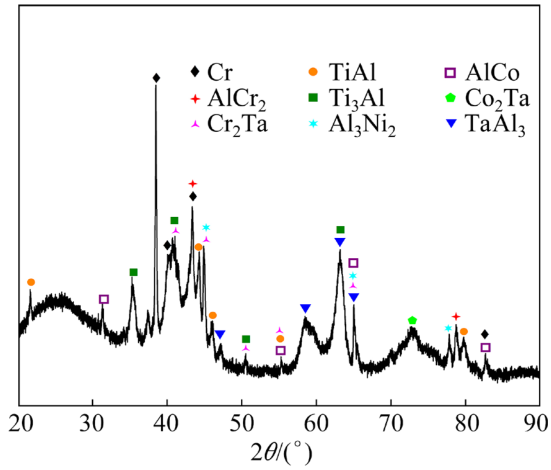

Fig. 1 XRD pattern of Cr/CoNiCrAlTaY coated specimen before oxidation

Figure 2 shows the surface and cross-sectional morphologies of the specimens. The top layer is composed of Cr grains with sizes ranging in 0.5−2 μm (Fig. 2(a)). The Cr top-layer exhibits an island-like morphology, a characteristic feature of coatings fabricated by PSMT, as reported for Mo [25] and Cr [26−30]. In contrast to MCrAlY (M= Ni, Fe, and Co) coatings deposited by thermal spraying [5] or additive manufacturing [31], the as-prepared coating displays a dense, crack-free structure with fine surface grains (Fig. 2(b)). The cross-sectional morphology (Fig. 2(c)) shows that the interface is free from delamination and/or microcracks. EDS line-scanning reveals that the top Cr layer (i) has a thickness of (3.8±0.5) μm, while the CoNiCrAlTaY transition layer (iii) measures as ~(6.0±0.3) μm. An interdiffusion zone (ii) forms between the Cr layer and the transition layer (Fig. 2(c_1)), and a similar interdiffusion zone (iv) develops between the transition layer and the substrate (Fig. 2(c_2)). These diffusion zones play a critical role in enhancing the adhesion of the Cr/CoNiCrAlTaY coating to the substrate. Notably, the intensity of Ta, as evidenced by counts per second (CPS), is higher at diffusion interfaces ii and iv than in the transition layer iii.

To gain a deeper understanding of the coating, the as-deposited specimens were characterized by TEM. Figure S1(a) in Supplementary Information (SI) shows the bright-field (BF) scanning TEM image, with an inset depicting the FIB-prepared foil. The transition layer, marked by a yellow box in Fig. 3(a), is further analyzed via elemental mappings (Fig. S1(b) in SI). Figure 3(a) shows the

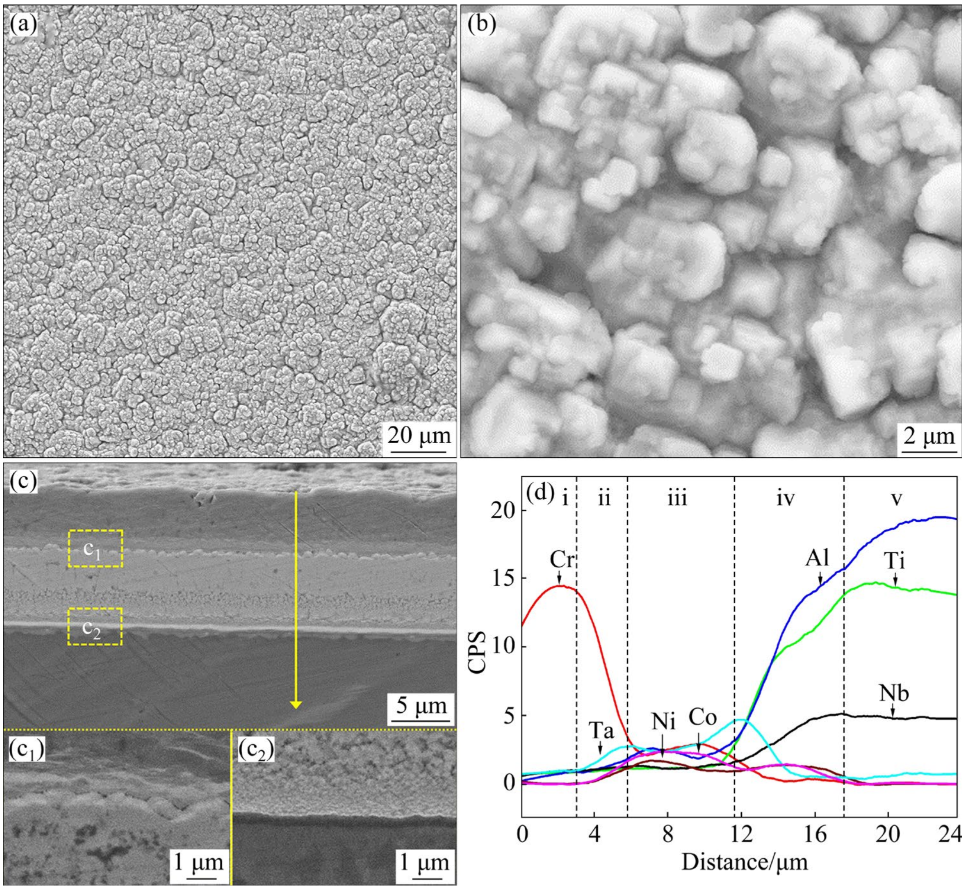

Fig. 2 SEM images of coating: (a, b) Surface morphology; (c−c$_2$) Cross-sectional morphologies of interface and transition layer−substrate interface; (d) Line-scanning result of (c)

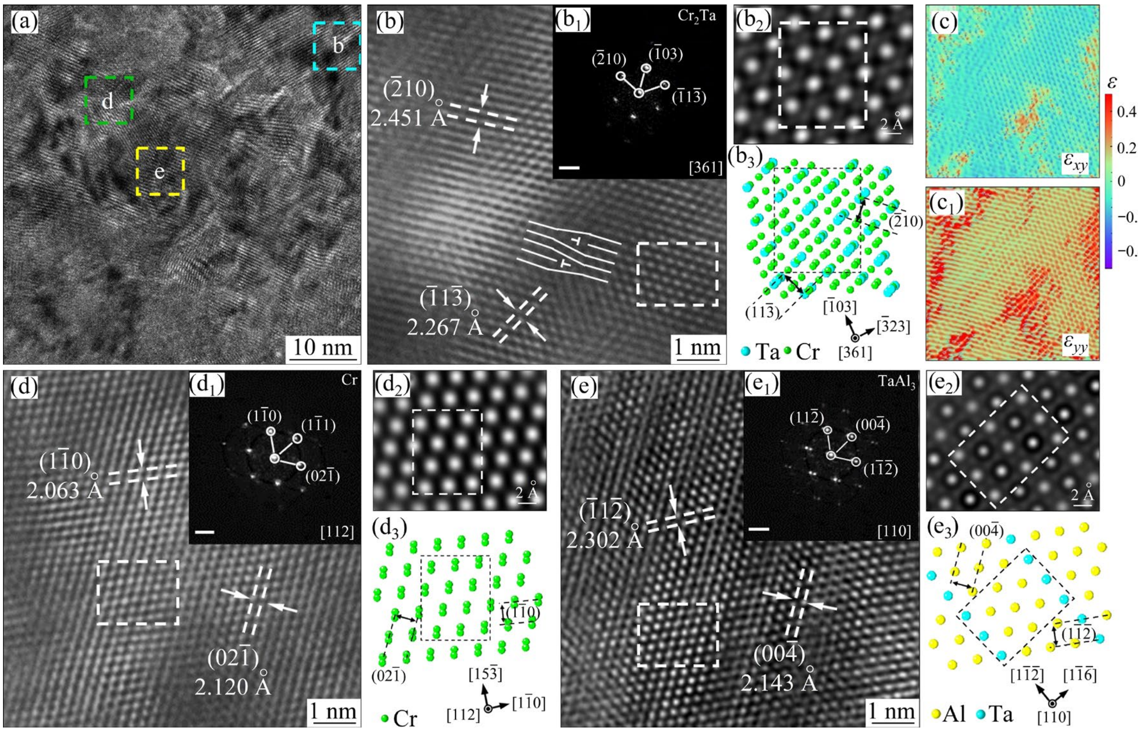

Fig. 3 HRTEM and FFT images of coating before oxidation: (a) Coating; (b, c) Cr_2Ta and strain maps; (d) Cr; (e) $TaAl_3$ (data from Fig. S1 in SI)

HRTEM image characterizing the structure of the CoNiCrAlTaY layer, corresponding to the marked region of Fig. S1(b) in SI. In the HRTEM image, *d*-spacing values of 0.245 and 0.227 nm were measured for Cr_2Ta $(\bar{2}10)$ and $(\bar{1}1\bar{3})$ in the interface-adjacent region (bright blue box), which were identified as Cr_2Ta by the [361] zone axis in the FFT image (Figs. 3(b), (b_1)). The simulated HRTEM image and atomic model verify the hexagonal (C14) structure and atomic arrangement of Cr_2Ta structure (Figs. 3(b_2), (b_3)). Cr_2Ta, a Laves phase, has a melting point above 2293 K, exhibiting a stable lattice structure at high temperature [32]. Moreover, precipitation and coarsening kinetics in the Cr−Ta system remain extremely sluggish even at 1473 K, indicating retarded diffusion [33].

Moreover, dislocations were observed at the Cr/CoNiCrAlTaY interface (denoted by T in Fig. 3(b)), indicating severe lattice mismatch and high strain concentration. Strain maps for ε_{xy} and ε_{yy}, obtained via geometric phase analysis (GPA), reveal the strain distribution around dislocations (Figs. 3(c), (c_1)). Similarly, Cr [112] in the top layer (Figs. 3(d)−(d_3)) and $TaAl_3$ [110] in the CoNiCrAlTaY layer (Figs. 3(e)−(e_3)) were identified using the same characterization approach. Studies have shown that $TaAl_3$ forms at a non-parabolic growth rate within 673−798 K during solid-state diffusion in the Al−Ta system [34].

The interface was free of voids (Fig. S2(a) in SI), which is consistent with previous findings [27−29]. EDS mapping analysis shows that Al distribution correlates well with Cr and Co, while Ta distribution is consistent with Al at the interface. Local regions near the interface in the HRTEM image were further analyzed (Fig. S2(b) in SI). $AlCr_2$ with [331] zone axis was identified from HRTEM lattice fringes (Fig. 4(a)) and FFT analysis (Fig. 4(a_1)) of the selected region (green boxes in Fig. S2(b) in SI). This identification was verified by its simulated HRTEM image (Fig. 4(a_2)) and atomic model (Fig. 4(a_3)). Additionally, $ArCo_4$ [001] in the CoNiCrAlTaY layer (Figs. 4(b)−(b_3)), and Ti_3Al [012] (Figs. 4(c)−(c_3)) and TiAl [111] (Figs. 4(d)−(d_3)) in the substrate were also identified.

3.2 Oxidation kinetics

Figure 5 shows the oxidation kinetics curves of the Cr/CoNiCrAlTaY coated specimens in static air at 1173 K for 200 h. The Ti−45Al−8.5Nb alloy exhibited a mass gain (Δm) of 1.7 mg/cm^2, in good

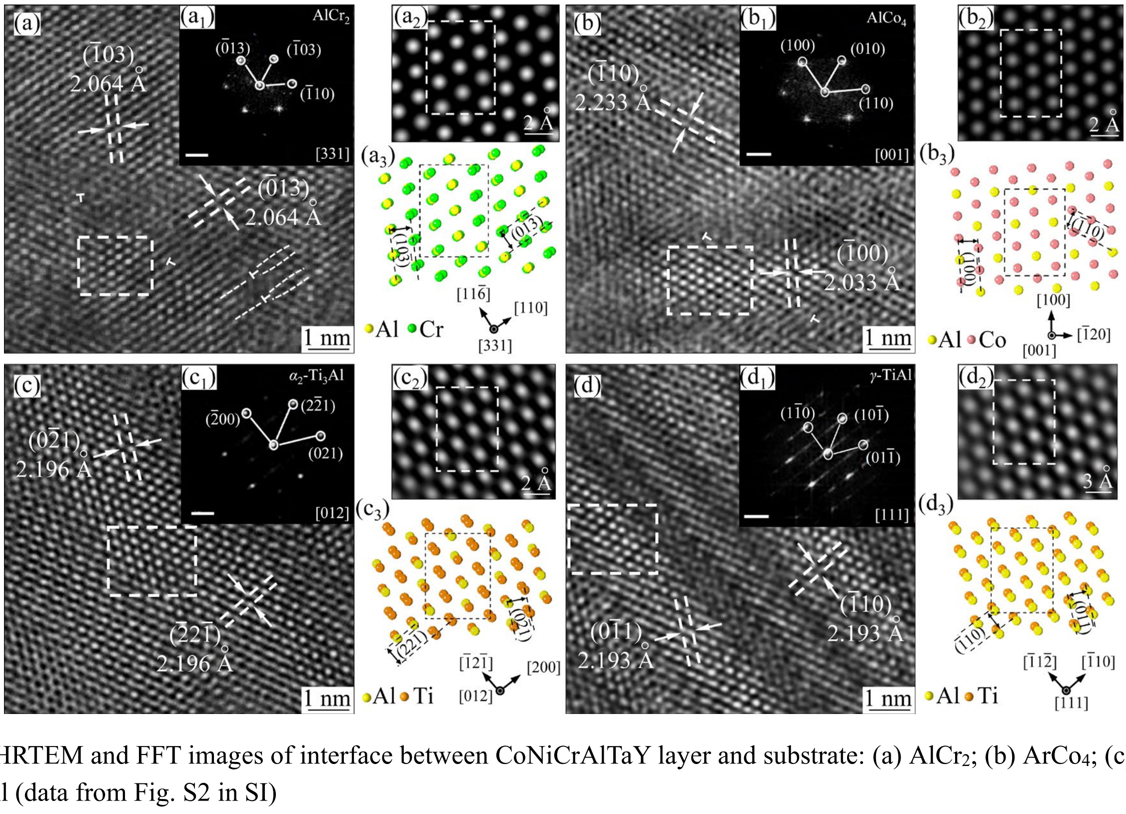

Fig. 4 HRTEM and FFT images of interface between CoNiCrAlTaY layer and substrate: (a) $AlCr_2$; (b) $ArCo_4$; (c) Ti_3Al; (d) TiAl (data from Fig. S2 in SI)

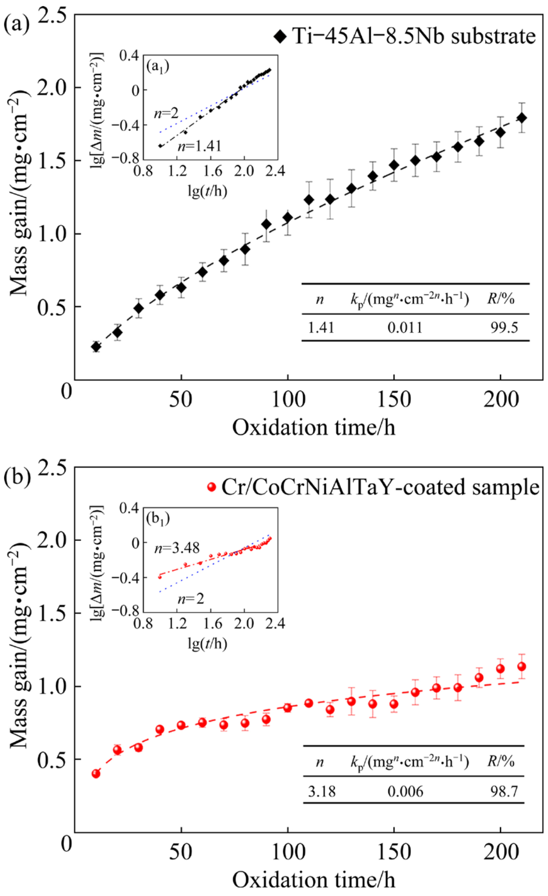

Fig. 5 Isothermal oxidation kinetic curves at 1173 K for 200 h: (a) Ti−45Al−8.5Nb alloy; (b) Cr/CoNiCrAlTaY coated specimen

agreement with previous studies [3,26]. By contrast, the Cr/CoNiCrAlTaY coated specimen showed a mass gain of 1.0 mg/cm^2. A power-law equation was used to describe the relationship between the mass gain and oxidation time [26−28,35]:

$$\Delta m/A = k_p t^n \tag{1}$$

where A represents the specimen area, t is the oxidation time, k_p is the oxidation rate, and n is the rate exponent. The n-value for the Ti−45Al−8.5Nb alloy was 1.41, obtained by fitting a logarithmic function (inset in Fig. 5(a$_1$)), R is the goodness of fit, and this value deviated from the parabolic law (n=2) of protective oxide films. Notably, the coated specimen exhibited n-value of 3.18, indicating that the enhanced oxidation resistance stemmed from not only retarded oxygen diffusion via the formed Cr_2O_3 protective layer but also oxidation and chemical reactions within the CoNiCrAlTaY coating.

3.3 Microstructure and cross-section evolution during thermal oxidation

Figure 6 presents the XRD patterns of the Cr/CoNiCrAlTaY coated specimens after oxidation at 1173 K in air. Notably, diffraction peaks from the oxide (i.e., Cr_2O_3), compounds (i.e., Cr_2Ta, AlNi, and $AlCo_2Ta$), and the substrate were indexed for oxidation time ranging from 1 to 50 h (Fig. 6(a)). This is attributed to the X-ray detection depth of 10−20 μm, corresponding to the depth of the Cr/CoNiCrAlTaY coating. Furthermore, the diffraction peaks of metallic phases disappeared with increasing oxidation time (i.e., 50 h). while the intensity of

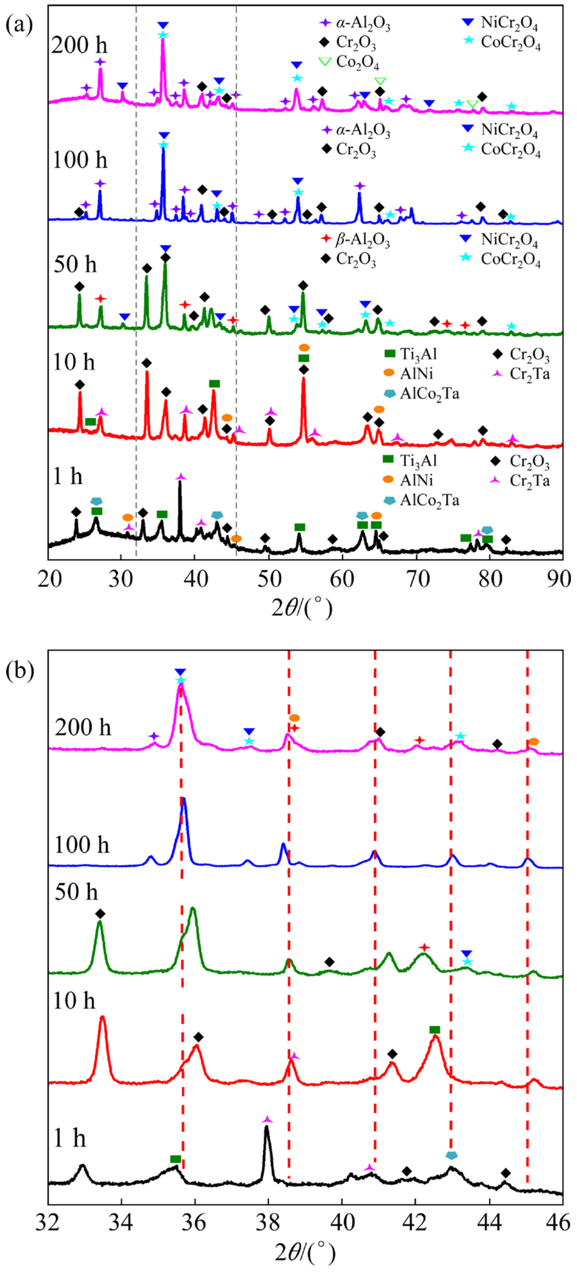

Fig. 6 XRD patterns of Cr/CoNiCrAlTaY coated specimens after oxidation

Cr_2O_3 diffraction peaks increased, particularly at 2θ of 24.49° and 36.20°, corresponding to the (012) and (110) crystal planes, respectively. This indicates that the formed Cr_2O_3 layer thickens with increasing oxidation time. Additionally, oxides such as Al_2O_3, $NiCr_2O_4$, and $CoCr_2O_4$ were identified by comparison with PDF standards. However, at oxidation time of 100 and 200 h, the Cr_2O_3 peak intensity decreased while that of Al_2O_3 increased. Notably, spinel oxides ($NiCr_2O_4$ and $CoCr_2O_4$) exhibited enhanced diffraction peaks intensity. Figure 6(b) shows the XRD result within 32°−46°, indicating that the diffraction peaks at ~35.8° and 38.5° shifted to lower 2θ values, which is associated with lattice parameter changes and thermal stress.

Figure 7 presents the surface morphologies of the Cr/CoNiCrAlTaY coated specimens after oxidation. Notably, fine oxide particles form on the surface after 10 h of oxidation (Figs. 7(a), (a_1)). In contrast to the as-prepared morphologies in Figs. 2(a) and (b), the specimen surface after 10 h of the oxidation is covered by dense Cr_2O_3 grains, specifically 13−290 nm in size. EDS mapping and point analysis (Table 1) reveal a uniform chemical composition, suggesting the formation of a stable Cr_2O_3 film. Gully-like regions contain fine Cr_2O_3 grains (Figs. 7(b), (b_1)). while the surface also features densely packed, sharply defined rhombus-shaped Cr_2O_3 oxides ranging from ~180 nm to 1.0 μm (Figs. 7(c), (c_1)). However, during prolonged oxidation at 200 h, the surface morphology exhibits intact and defective regions (marked by iv and v in Fig. 7(d)). Notably, 1−3 μm holes form among the oxides in the defective region (Fig. 7(d_1)). Table 1 shows that the oxides are rich in O and Cr, with trace Ni and Co elements. This suggests that a Cr_2O_3 film forms during initial oxidation, which later evolves spinel compound films ($NiCr_2O_4$ and $CoCr_2O_4$) as oxidation time increases.

The cross-sectional images and chemical composition of the Cr/CoNiCrAlTaY coated specimens after isothermal oxidation are shown in Fig. 8. The O and Cr chemical elements indicate that a continuous Cr_2O_3 film forms on the outermost layer after 100 h of oxidation (Fig. 8(a)), which is in agreement with the surface composition (Figs. 8(a)−(a_6) and Table 1). The intermediate layer is composed of mixed oxides (Al_2O_3, $NiCr_2O_4$, and $CoCr_2O_4$) formed by oxidation of Al, Ni, Cr, Co and O. As oxidation time increases (Fig. 8(b) and element distribution maps), continuous Al_2O_3 layers are observed immediately beneath the uppermost Cr_2O_3 film, as confirmed by O and Al distribution analysis. Moreover, Ti diffuses toward the CoNiCrAlTaY transition layer but does not penetrate the Cr_2O_3 film surface (Figs. 8(b_1)−(b_6)). Ni and Co diffuse toward the outer layer and substrate, with their diffusion layers maintaining a consistent thickness of 3 μm.

3.4 Adhesion

Figure 9 shows the adhesion properties and scratch morphologies of the coated specimens. The initial break force (L_{c1}) and peel-off force (L_{c2}) of the coatings were determined based on the sudden increase in the acoustic signal. Specimens before isothermal oxidation exhibited a sharp peak at 192 N (Fig. 9(a)), indicating strong adhesion. Numerous microcracks perpendicular to the scratch direction were observed in the surface morphology prior to the sudden change in the acoustic signal (Fig. 9(a_1)). Moreover, the Cr layer (Point 1 in Fig. 9(a_2), and chemical composition in Table 2) and the CoNiCrAlTaY layer covered the entire scratched surface, attributed to their good plasticity and toughness. By contrast, several spalling zones (marked in Fig. 9(a_3)) formed at the interface between the scratch and the surface (marked by the yellow dashed line) near the scratch end. Chemical composition analysis of Point 2 revealed that the spalling zone exposed substrate. During coating deposition, the substrate surface was bombarded by numerous argon ions, inducing vacancies and defects [21]. Consequently, pre-sputtered metal ions from the target penetrated the substrate surface and readily formed a gradient diffusion layer, contributing to the high adhesion strength between the coating and substrate [26−29].

By contrast, the L_{c1} and L_{c2} values for the specimens after 100 h of oxidation were 140 and 173 N (Fig. 9(b)), respectively. Both L_{c1} and L_{c2} decreased as oxidation time increased (Fig. 9(c)). The adhesion forces of the specimens were higher than those of the Cr coatings [26]. Moreover, the scratch was covered with Cr_2O_3 (Points 3 and 9). The high Cr content in the spalling zone (Points 4

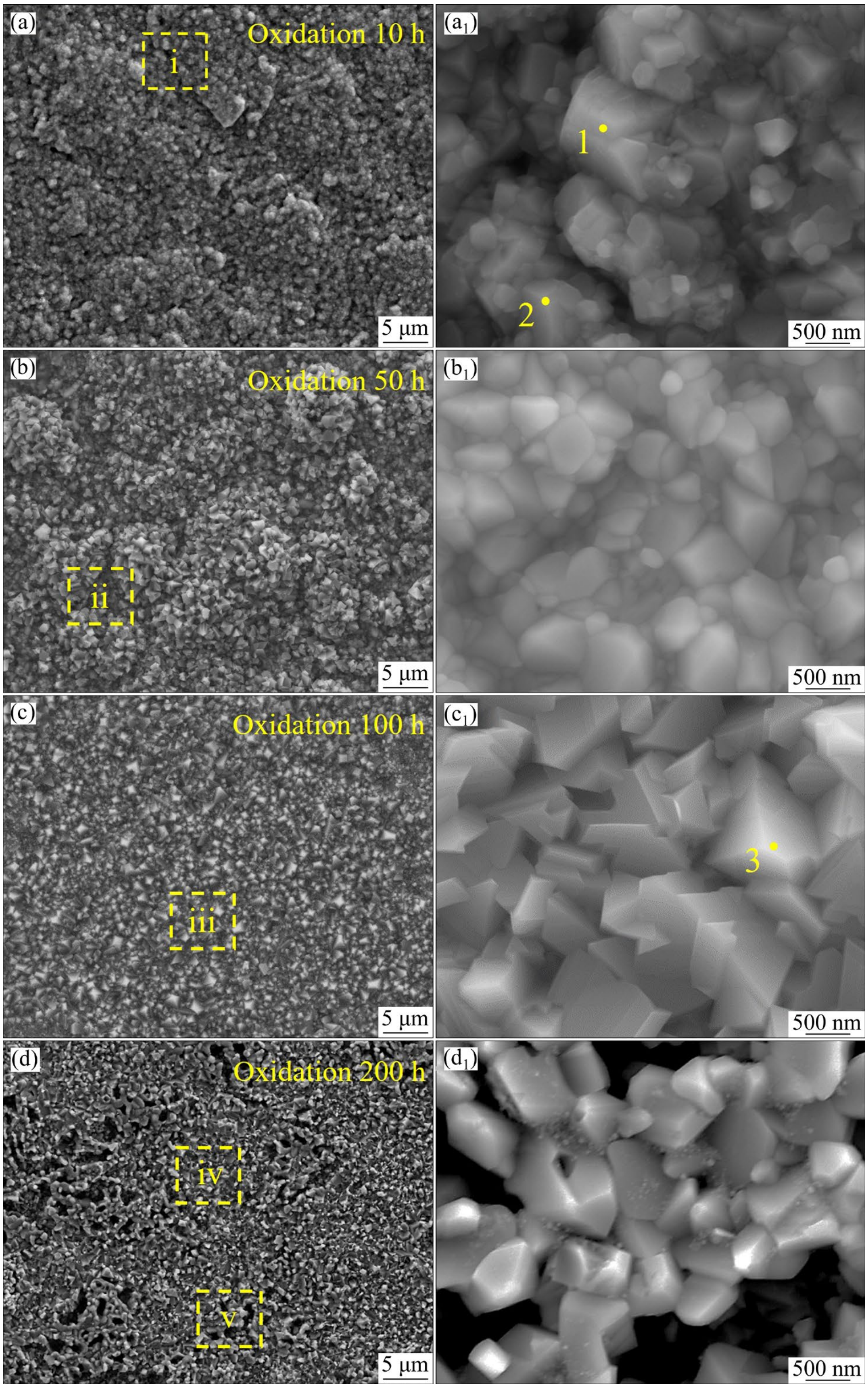

Fig. 7 SEM and high magnification images of coated specimens after oxidation at 1173 K in air for 10 h (a, a_1), 50 h (b, b_1), 100 h (c, c_1), and 200 h (d, d_1)

and 5) and the scratch (Point 6) indicated the presence of the Cr metal and/or its compounds. However, chemical composition analysis at Points 7 and 8 suggested that the spalling zone consisted of the CoNiCrAlTaY layer and the substrate. In addition to Cr_2O_3 (Point 9) in the scratch, the involved elements involved in the layers exhibited Cr-rich but non-stoichiometric characteristics (Point 10), indicating that the coating was not completely oxidized after 200 h of oxidation. Similarly, the

Table 1 Chemical compositions of Cr/CoNiCrAlTaY coated specimens before and after oxidation for 1−200 h tested by EDS mapping (M) and point analysis (P) (data from Figs. 2(b), 7 and 8) (at.%)

Time/h	Area	O	Cr	Al	Co	Ni	Ti	Ta	Nb
0	M	−	99.4	0.6	−	−	−	−	−
10	M-i	64	35.4	0.6	−	−	−	−	−
	P-1	64	35.7	0.3	−	−	−	−	−
50	M-ii	60.1	38.8	0.1	0.2	0.1	0.5	−	−
	P-2	64.4	35.1	0.3	−	−	−	−	−
100	M-iii	63.7	29.9	1.6	3.2	1.6	−	−	−
	P-3	63	32.6	0.2	3.5	0.5	0.2	−	−
	P-4	12.1	−	35.2	6.1	7.2	33.5	−	5.9
	P-5	2.3	0.5	43.8	6.8	9.1	25.9	−	11.5
200	M-iv	60.2	36.6	0.9	1.3	1	−	−	−
	M-v	42.3	19.6	2.6	14.2	18.6	2.3	0.4	−

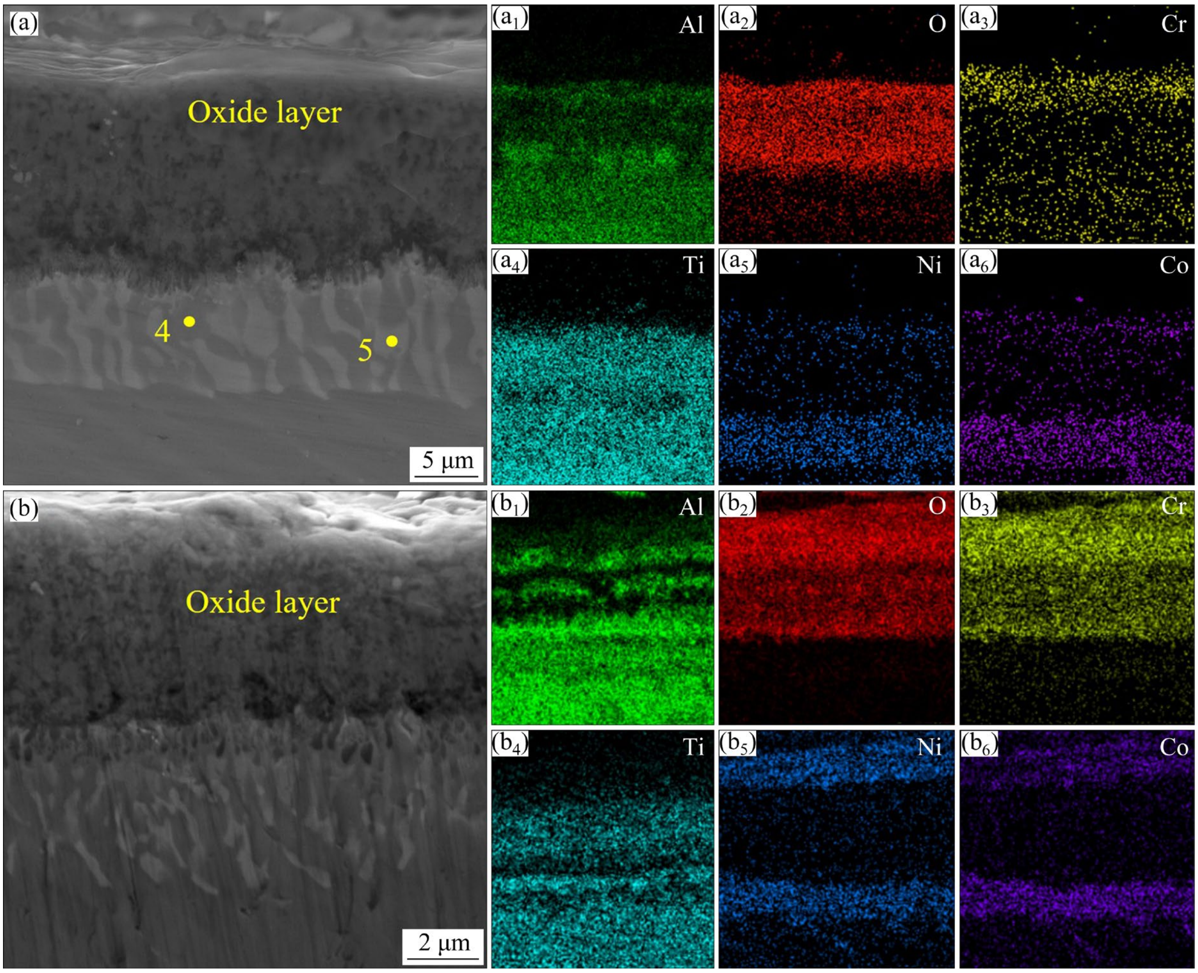

Fig. 8 SEM cross-sectional images of Cr/CoNiCrAlTaY coated specimens after oxidation and elemental distribution: (a) 100 h; (b) 200 h

elements at Point 11 on the scratch belonged to the CoNiCrAlTaY layer, whereas Point 12 in the spalling zone originated from the substrate.

3.5 Interface of coating/substrate during oxidation

Figure 10 presents the TEM BF images of the coated specimen after 10 h of oxidation. Figure 10(a)

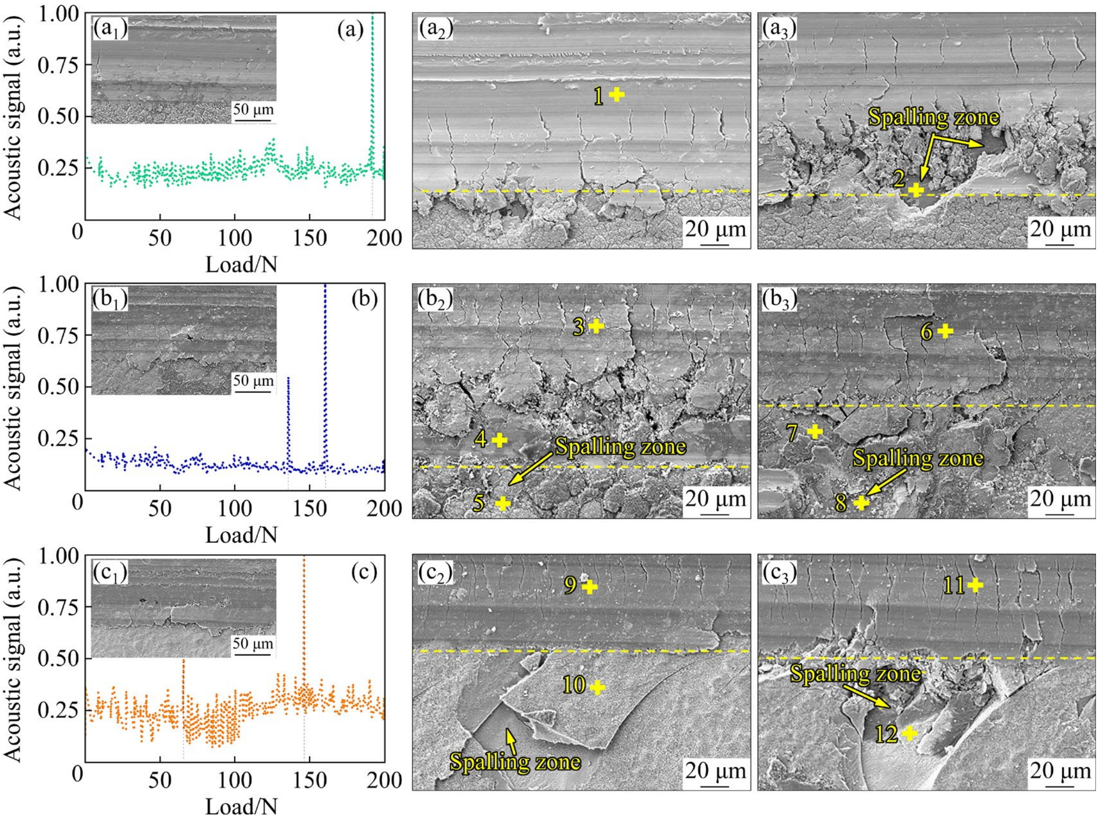

Fig. 9 Scratch test results and SEM images of Cr/CoNiCrAlTaY coated specimens after isothermal oxidation: (a) 0 h; (b) 100 h; (c) 200 h

Table 2 Chemical compositions of marked Points 1−12 in Fig. 9 by EDS-pointing scan analysis (at.%)

Time/h	O	Cr	Al	Co	Ni	Ti	Ta	Nb
0	4.2	92.1	1.4	−	−	1.5	0.7	−
	−	0.6	39	11.3	8.3	34	−	6.8
100	54.9	30.9	6.4	1.2	0.8	4	1.8	−
	10.3	85.5	1.3	−	−	2	0.9	−
	28.5	68.8	1.3	−	−	1.4	−	−
	45.2	46	4.9	−	−	3.5	0.4	−
	18.6	1.8	32.1	7.1	5	25	−	10.4
	7.3	3.4	6.2	23.6	8.5	49.1	−	1.8
200	68.7	29.1	1.3	−	−	0.9	−	−
	27.4	46.8	2.9	16	4	1.4	1.5	−
	38.5	28.5	7.4	6.4	4.6	11.4	3.2	−
	−	1	50.4	7.4	7.3	26.1	−	7.8

shows the HRTEM image of the region marked by a yellow box in the inset, which indicates a distinct boundary. A particle-like precipitate with a size of ~110 nm is observed (Fig. 10(b)), and is identified as Ta_2O_5 $[\bar{1}01]$ via *d*-spacing measurement from HRTEM (Fig. 10(c) and FFT analysis (Fig. 10(c₁)). The selected region (blue box in Fig. 10(c)) is shown in the simulated HRTEM image and its atomic arrangement model (Figs. 10(c₂), (c₃)), further confirming Ta_2O_5. Additionally, GPA strain

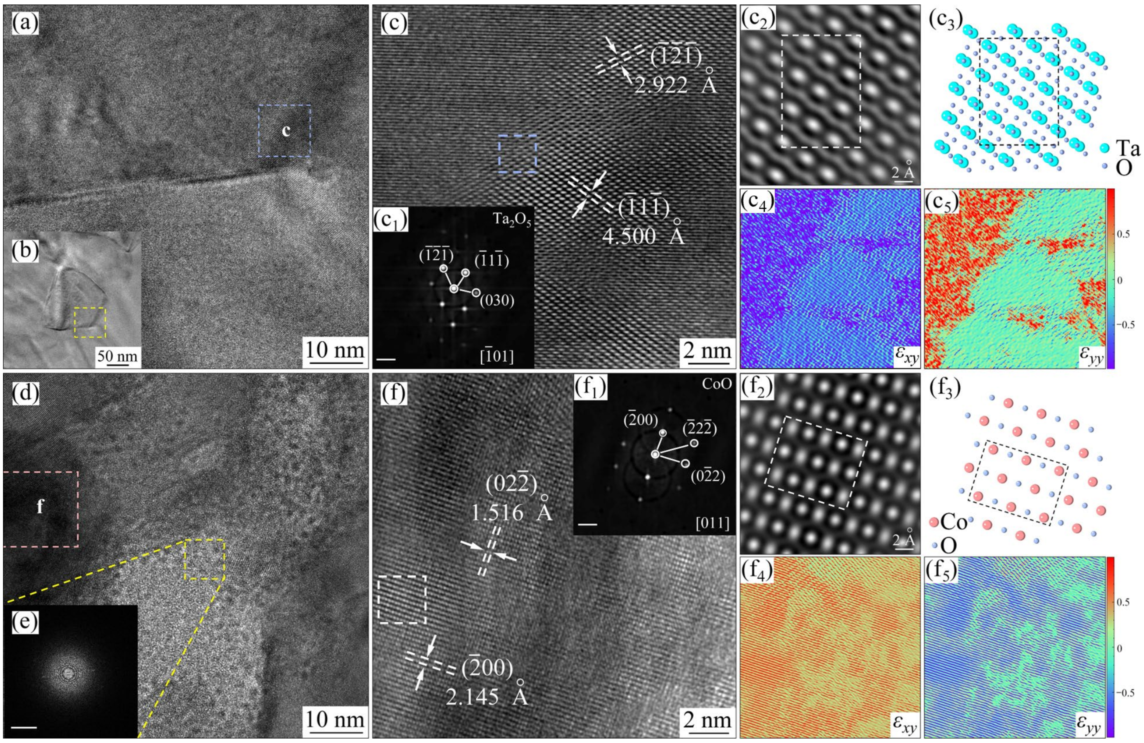

Fig. 10 TEM images of Cr/CoNiCrAlTaY coating after oxidation for 10 h: (a, b) HRTEM image of coating; (c) HRTEM image and corresponding strain maps of Ta_2O_5; (d, e) HRTEM and FFT images of coating; (f) HRTEM image and corresponding strain maps of CaO

maps for ε_{xx} and ε_{xy} reveal local strain in the vicinity (Figs. 10(c_4), (c_5)). The region marked by a yellow box in Fig. 10(d) is identified as an amorphous structure based on the FFT image (Fig. 10(e)), attributed to the PSAT fabrication process. The presence of an amorphous phase and metastable oxides aligns with the XRD results for the short-term oxidation. The pink-boxed region in Fig. 10(d) is indexed as CoO [011] via FFT analysis (Fig. 10(f_1)) and *d*-spacing values, as shown in the HRTEM image (Fig. 10(f)). CoO is further confirmed by its simulated HRTEM and atomic model (Figs. 10(f_2), (f_3)). GPA analysis indicates a non-uniform strain distribution (Figs. 10(f_4), (f_5)).

Figure 11 shows the HRTEM and FFT images of the oxide scale and subsurface region of the Cr/CoNiCrAlTaY coated specimen after oxidation at 1173 K for 100 h. The top layer consists of the Cr_2O_3 scale, beneath which several dark precipitates (5–28 nm in size) are observed (Fig. S3(a) in SI). HRTEM characterization of the interfacial region marked by green and yellow boxes Fig. S3(a) in SI is shown in Figs. 11(a, b). $CrCo_2O_6$ [011] and $YAlO_3$ [354] are confirmed by their HRTEM images, atomic models, and simulated HRTEM images, validated by crystal fringe measurements and FFT calibration (inset in Figs. 11(a, b)). Additionally, Figure S3(b) in SI reveals a local precipitate region at the interface with its elemental distribution. Figure 11(c) shows the precipitate-containing region (purple box in Fig. S3(a) in SI), where precipitates are located at grain boundaries. Two regions around the precipitate (purple and bright-blue boxes in Fig. 11(c)) are identified as spinel oxides Al_2NiO_4 [051] and Ta_2O_3 $[\bar{2}11]$ (Figs. 11(d, e)). GPA strain and distortion maps of the interface region (Figs. 11(c_1−c_4)) indicate the presence of shearing strains (ε_{xy}) and distortions (ε_{yy}).

According to Figs. 1, 3 and 4, Cr/CoNiCrAlTaY coated specimens consist of a top Cr layer and multiple phases in the subsurface CoNiCrAlTaY layer, where the Ta-containing phases are identified as Cr_2Ta and $TaAl_3$. The coated alloy exhibits improved oxidation resistance and strong adhesion (Figs. 5 and 9). The uniform Cr_2O_3 surface and microcrack-free interface indicate that the coating restricts the diffusion of oxygen ions and retards interdiffusion among the oxide among the oxide scale, coating, and substrate (Figs. 6−8). Moreover,

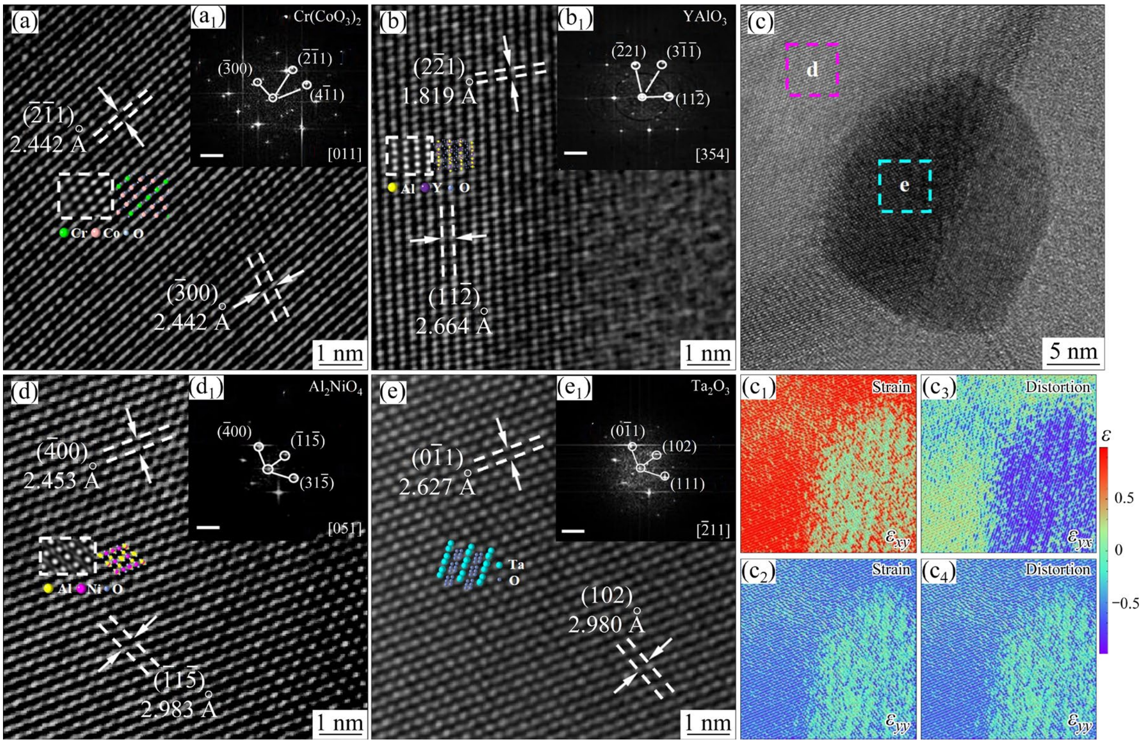

Fig. 11 HRTEM and FFT images of coated specimens after oxidation at 1173 K for 100 h: (a) $Cr(CoO_3)_2$; (b) $YAlO_3$; (c) HRTEM image and strain maps of oxide scale in Cr/CoNiCrAlTaY coating; (d) $NiAl_2O_4$; (e) Ta_2O_3 (data from Fig. S3 in SI)

the outward diffusion of elements (Al, Ni and Co) initiates voids in the Cr_2O_3 layer with the increasing oxidation time and forms spinel oxides ($CoCr_2O_4$, and Al_2NiO_4), as confirmed by TEM and HRTEM results (Figs. 11(a) and (d)). The Ta oxides are further identified as Ta_2O_5 $[\bar{1}01]$ and Ta_2O_3 $[\bar{2}11]$.

4 Discussion

The oxidation of *γ*-TiAl alloy is almost always accompanied by the poor spalling resistance of the oxide scale, which is attributed to competitive growth between TiO_2 and Al_2O_3 [3−6], thereby limiting the actual service temperature [36]. In this study, the Cr/CoNiCrAlTaY-coated TiAl alloy exhibits superior oxidation resistance compared to the substrate at 1173 K.

Figure 12 illustrates a schematic diagram of oxidation, interdiffusion and degradation, which can roughly define the following processes based on the chemical reaction between oxygen and elements in contact. In the early oxidation stage (I→II), the adsorbed oxygen (O_2, Stage I) starts to react with Cr atoms to form Cr_2O_3. The chemical reaction occurs in the Cr film at 1173 K in a muffle furnace under air. Thermodynamic data are obtained using an Ellingham-Richardson diagram [37,38], according to the following equation:

$$Cr(s)+O_2(g)\rightarrow Cr_2O_3(s) \tag{2}$$

where the standard Gibbs free energy ($\Delta G^{\ominus}$) is −815.2 kJ/mol (Fig. 13). When a continuous Cr_2O_3 film forms (Stage II→III), the oxidation mass gain rate is determined by diffusion along the grain boundary, as described by Eq. (2), until the Cr layer is consumed and oxidized to form the Cr_2O_3 film (Stage II), as marked as i in Fig. 13. Then, more elements are involved in the chemical reactions between the Cr_2O_3 and the CoNiCrAlTaY layer, as illustrated in the following equation:

$$Cr_2O_3(s)+M(s)+O_2(g)\rightarrow MCr_2O_4(s) \tag{3}$$

where M denotes Ni and Co elements. Due to the outward diffusion of Ni and Co, Cr_2O_3 reacts with Ni and Co to form $NiCr_2O_4$ and $CoCr_2O_4$, as labeled ii in Fig. 13. The formation of these spinel oxides aligns with the XRD results in Fig. 6. Moreover, Al can be oxidized owing to the negative $\Delta G^{\ominus}$ (−1298.1 kJ/mol), yet its low concentration leads to stable oxidation (Stage III). The chemical reaction is as follows:

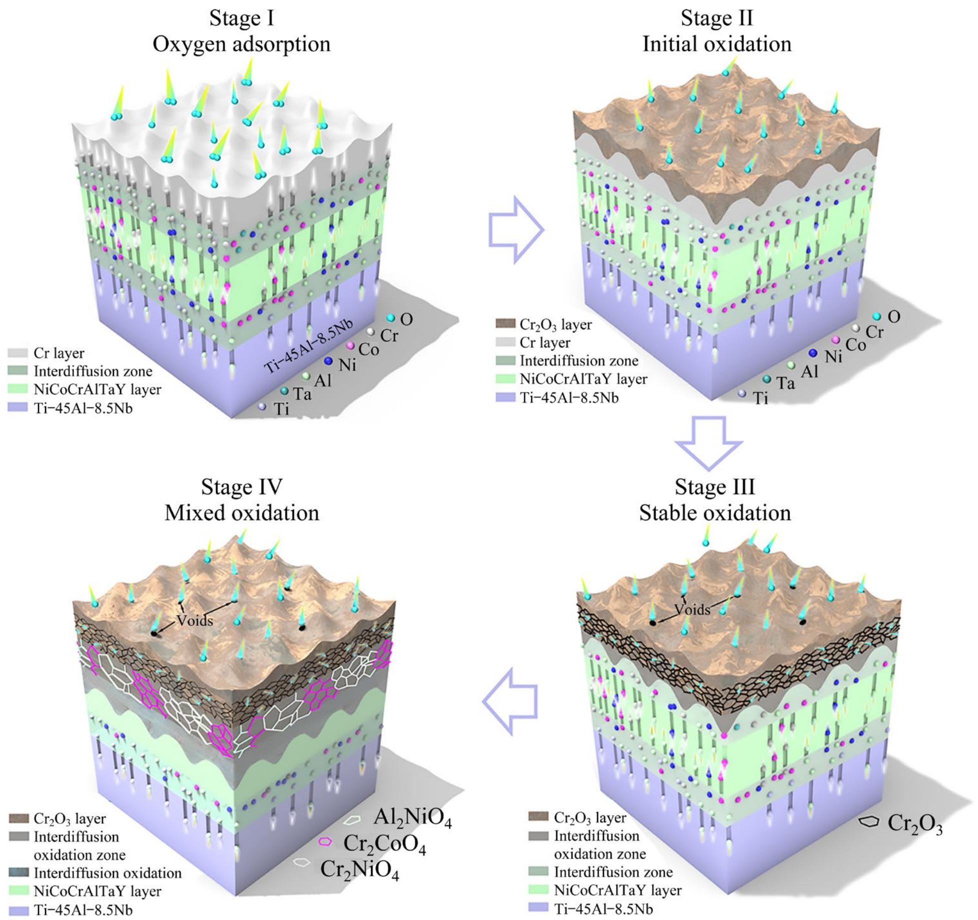

Fig. 12 Schematic diagram of Cr/CoNiCrAlTaY coating on Ti−45Al−8.5Nb substrate

$$Al(s)+O_2(g)\rightarrow Al_2O_3(s) \tag{4}$$

With prolonged oxidation, the interdiffusion of elements involved and oxidation results in oxide phase transformation (Stage III→IV), as marked by Stages III and IV in Fig. 12. This includes at least three types of chemical reactions: (i) oxygen reacts with M (Eq. (5)), (ii) metals, including M and N (Cr and Al), react with oxygen (Eq. (6)), and (iii) reactions between N_2O_3 oxides (e.g., Cr_2O_3 and Al_2O_3) and MO oxides (e.g., CoO, NiO) (Eq. (7)), as shown in Figs. 10(f) and 11(c, h). In addition, despite the high oxidation reactivity of Ta (Ta_2O_5, $\Delta G^{\Theta}=-1530$ kJ/mol) and Y (Y_2O_3, $\Delta G^{\Theta}=-1569$ kJ/mol), Ta and Y have lower concentrations and slower diffusion rates than other metals (Co, Ni and Cr), thus influencing the chemical reactions in Stages III and IV. The chemical reactions are marked as iii in Fig. 13.

$$M(s)+O_2(g)\rightarrow MO(s) \tag{5}$$

$$M(s)+N(s)+O_2(g)\rightarrow MN_2O_4(s) \tag{6}$$

$$MO(s)+N_2O_3(s)+O_2(g)\rightarrow MN_2O_4(s) \tag{7}$$

The strong adhesion arises from metallurgical bonding during coating deposition and interdiffusion among the Cr/CoNiCrAlTaY/alloy. The diffusion coefficient of Cr on the Ti−45Al−8.5Nb alloy is ~1×10^{-4} μm²/s at 1073 K during PSMT fabrication [26]. Argon plasma bombardment of the *γ*-TiAl substrate during deposition creates high-concentration surface vacancies with a gradient distribution [21]. This bombardment also heats the substrate to the target temperature. Facilitated by high-temperature vacancy diffusion, robust adhesion is achieved, as shown in Fig. 9(a), consistent with prior reports: L_c values of 145 N for Cr coatings [26] and 172 N for CoNiCrAlTaY on Ti−45Al−8.5Nb [27]. Following continuous Cr_2O_3 film formation, O and Cr diffusion coefficients decrease to ~1×10^{-7} and 1×10^{-8} μm²/s at 1073 and 1273 K, respectively. The CoNiCrAlTaY/*γ*-TiAl interface shows no delamination even after 200 h. Furthermore, TEM analysis identifies Ta-rich phases (C14 Cr_2Ta and $TaAl_3$) in the CoNiCrAlTaY coating (Fig. 3) and Ta oxides (Ta_2O_5/Ta_2O_3) after thermal oxidation (Figs. 10 and 11), indicating high-temperature oxidation of Ta-rich phases via Cr_2Ta (or $TaAl_3$)→Ta_2O_5 (and/or Ta_2O_3). Figure 14 depicts the atomic structure and oxidation process. The Cr_2Ta features a primary cubic ($Fd\bar{3}m$, C15) phase and hexagonal (P_{63}/mmc, C14 and C36) phase with Cr_I/Cr_{II} sites (dash red circle in Fig. 14). Metastable C14 transforms to C15 via C36 with composition adjustments [39]. Diffusion coefficient of Cr atoms exceeds that of Ta by 2−3 orders of magnitude under pre-existing Cr/Ta vacancies [32], making Cr_2Ta diffusion Cr-controlled. Thus, Cr atoms in micron-sized Cr_2Ta migrate during high-temperature oxidation, forming an outer Cr_2O_3 layer and enhancing oxidation resistance [40,41]. The diffused Cr atoms create vacancies that facilitate O diffusion into the alloy (Fig. 14). TEM image confirms Ta oxides (Ta_2O_5/Ta_2O_3) after oxidation (Figs. 10(c) and 11(e)). In comparison, $TaAl_3$ belongs to the $I4/mmm$ space group (prototype, $TiAl_3$) [42]. with Al_I/ Al_{II} sites versus a single Ta site (Fig. 14). Due to the high diffusivity of Al, $TaAl_3$ can form even below 773 K [35,43]. Additionally, the Ta/Al coating exhibits improved oxidation resistance on IMI 834 titanium alloy at 1073 K. Although the Al−33Ta alloy exhibits good oxidation resistance due to outward diffusion of Al atoms, which forms a protective Al_2O_3 film during initial oxidation above 1173 K, the rapid diffusion of Al coupled with sluggish Ta mobility leads to subsurface voids, cracks, and oxidation degradation after prolonged exposure [44,45].

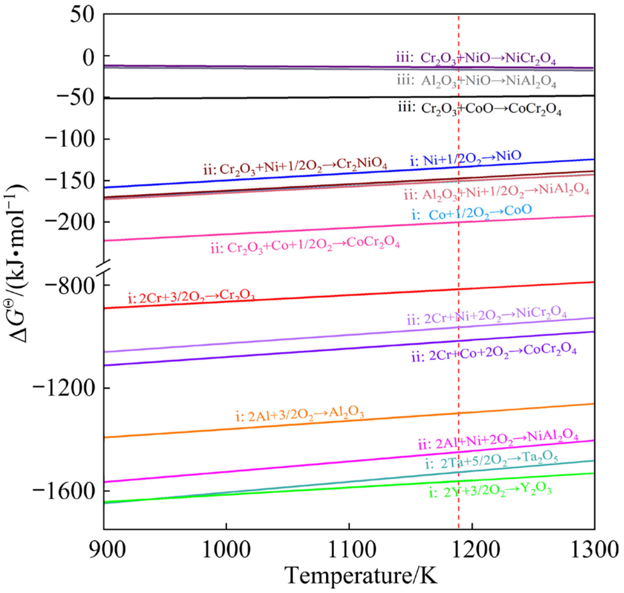

Fig. 13 Standard Gibbs free energy change with temperature of possible oxides

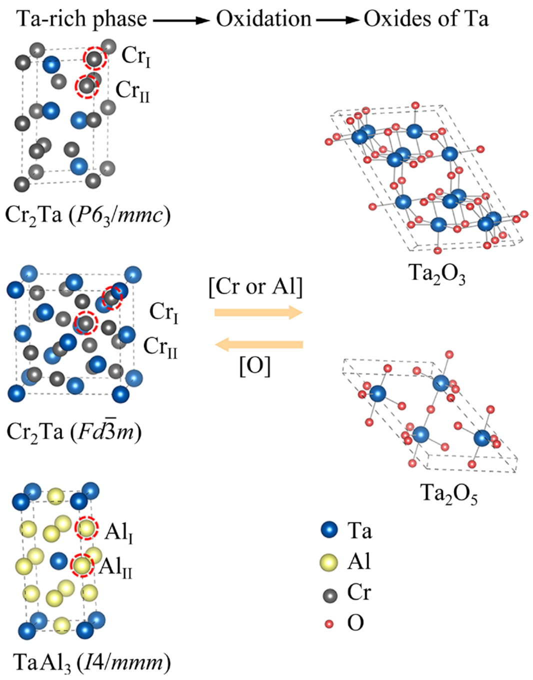

Fig. 14 Atomic structure and oxidation process

During high-temperature oxidation, the formation of voids and microcracks in the oxide scale is closely associated with oxide growth and thermal stresses. Thermal stress σ_c induced by the mismatched thermal expansion can be expressed as follows [46,47]:

$$\sigma_c = \frac{E_c}{1-\nu_c}\int_{298}^{1173}(\alpha_s-\alpha_c)\mathrm{d}T \tag{8}$$

where E_c and ν_c denote the elastic modulus and Poisson's ratio, respectively, α_s and α_c represent the temperature-dependent expansion coefficients (CTEs) of the coatings (Cr_2O_3, MCrAlY) and γ-TiAl substrate, respectively. The CTE of Cr_2O_3 increases from 4.2×10^{-6}/K at room temperature to 7.7×10^{-6}/K at 1173 K [47], whereas that of MCrAlY rises from 14.3×10^{-6} to 17.1×10^{-6}/K over the same temperature range [48,49]. Furthermore, the CTE value of the γ-TiAl alloy increasing from 9.7×10^{-6}/K at 298 K to 12.1×10^{-6}/K at 1173 K [50]. Using Eq. (6), σ_c was calculated for both Cr_2O_3 and MCrAlY. At 1173 K, the MCrAlY layer experiences a significant compressive stress of −3.54 GPa, consistent with reported values for Fe−46Ni−24Cr−4.8Al−0.05Y and Ni−20Cr−12.6Al−0.11Y [51]. Previous studies have shown that compressive stress suppresses microcrack formation and propagation during thermal cycling [52]. In contrast, the Cr_2O_3 scale harbors residual tensile stress of ~1.19 GPa (Fig. 15), which drives void and microcrack formation [47]. Notably, after 200 h of oxidation, voids form in the oxide scale but not in the CoNiCrAlTaY coating (Fig. 11(d)).

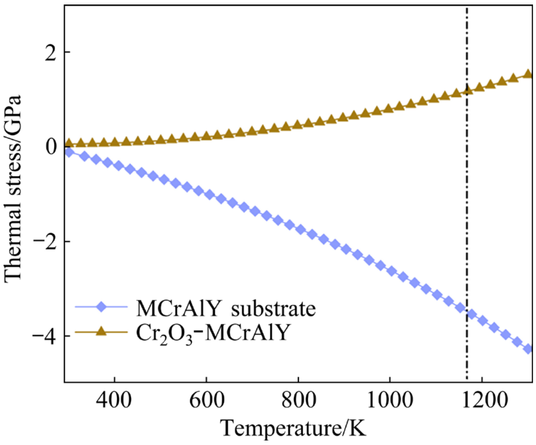

Fig. 15 Residual stress of Cr_2O_3 and MCrAlY layers of current coating deposited on Ti−45Al−8.5Nb alloy at high-temperature oxidation

Overall, the oxidation process of the Cr/ CoNiCrAlTaY coated specimens involves initial oxidation of the top Cr layer, followed by stable and mixed oxidation stages (Fig. 12). This oxidation is accompanied by oxide formation (Fig. 13) and increasing residual stresses (Fig. 15), driving the evolution of oxide structure, morphology, and adhesion properties (Figs. 6, 7 and 9). Extensive studies on MCrAlY/TiAl alloys have shown that refractory metals (i.e., Mo, Re, Hf, W and Ta) modified-MCrAlY (M=Ni, Co) coating suppress interdiffusion and enhance oxide scale adhesion [16,17]. Ta-rich phases, including $TaAl_3$ [110] and Cr_2Ta [361], are further oxidized to Ta_2O_5 $[\bar{1}01]$ and Ta_2O_3 $[\bar{2}11]$ (Figs. 10(c) and 11(e)). Cr_2Ta significantly restricts interdiffusion and improves oxidation resistance.

5 Conclusions

(1) The coating consisted of a Cr top layer, CoNiCrAlTaY deposited layer and diffused layers. Compounds such as Cr_2Ta, $AlCr_2$ and $AlCo_4$ formed near the interface. Moreover, the crack-free bilayer coating exhibited robust adhesion caused by metallurgical bonding during fabrication.

(2) The coated specimens exhibited good oxidation resistance at 1173 K. The Cr layer was oxidized on the Cr_2O_3 film with a low oxidation reaction rate. With the extended oxidation time, spinel oxides such as $NiCr_2O_4$ and $CoCr_2O_4$ formed due to the diffusion of Ni and Co toward the surface.

(3) The Ta-containing phases were identified as Cr_2Ta and $TaAl_3$ precipitates by HRTEM, and the Ta-oxide nanoparticles were indexed as Ta_2O_5 and Ta_2O_3, which played an essential role in improving the rapid diffusion, adhesion, and oxidation resistance of the oxide scale/coating/substrate.

CRediT authorship contribution statement

Zhen ZENG: Investigation, Methodology, Writing − Origin draft, Writing − Review & editing; **Yong-sheng WANG:** Investigation, Conceptualization, Funding acquisition, Supervision, Writing − Review & editing; **Ya-rong WANG:** Conceptualization, Methodology, Data curation and analysis, Visualization; **Bing ZHOU:** Supervision, Methodology, Funding acquisition; **Ke ZHENG:** Project administration; **Wan-yuan GUI:** Validation, Supervision; **Yan-li WANG:** Supervision; **Sheng-wang YU:** Investigation, Methodology, Funding acquisition; **Jun-pin LIN:** Investigation, Methodology.

Declaration of competing interest

The authors declare that they have no known competing financial interests or personal relationships that could have appeared to influence the work reported in this paper.

Acknowledgments

The authors would like to acknowledge financial supports from Shanxi Provincial Natural Science Foundation, China (No. 20210302123162), Shanxi Scholarship Council of China (No. 2024-057), State Key Laboratory of Advanced Metal Materials, China (No. 2019-ZD02), Science and Technology Achievement Transformation and Cultivation Project of Shanxi, China (No. 2020CG011), and Shanxi “1331 Project” Quality Improvement and Efficiency Project, China.

Supplementary Information

Supplementary Information in this paper can be found at: http://tnmsc.csu.edu.cn/download/08-p1837-2023-1171-Supplementary_Information.pdf.

References

[1] POLLOCK T M. Alloy design for aircraft engines [J]. Nature Materials, 2016, 15: 809−815.

[2] CHEN Guang, PENG Ying-bo, ZHENG Gong, QI Zhi-xiang, WANG Min-zhi, YU Hui-chen, DONG Cheng-li, LIU C T.

Polysynthetic twinned TiAl single crystals for high-temperature applications [J]. Nature Materials, 2016, 15: 876−881.

[3] LI Xiao-bing, XU Hao, XING Wei-wei, CHEN Bo, SHU Lei, ZHANG Meng-shu, LIU Kui. Microstructural evolution and mechanical properties of forged β-solidified γ-TiAl alloy by different heat treatments [J]. Transactions of Nonferrous Metals Society of China, 2022, 32: 2229−2242.

[4] LU Wei, CHEN Chun-lin, HE Lian-Long, WANG Fu-hui, LIN Jun-pin, CHEN Guo-liang. (S)TEM study of different stages of Ti−45Al−8Nb−0.2W−0.2B−0.02Y alloy oxidation at 900 °C [J]. Corrosion Science, 2008, 50: 978−988.

[5] MOSKAL G, NIEMIES D, CHMIELA B, KAŁAMARZ P, DUREJKO T, ZIĘTALA M, CZUJKO T. Microstructural characterization of laser-cladded NiCrAlY coatings on Inconel 625 Ni-based superalloy and 316L stainless steel [J]. Surface and Coatings Technology, 2020, 387: 125317−125328.

[6] PAN Yang-yang, LIANG Bo, HONG Du, HAN Di-juan, ZHONG Xin, NIU Ya-ran, ZHENG Xue-bin. Effect of TiAlCrNb buffer layer on thermal cycling behavior of YSZ/TiAlCrY coatings on γ-TiAl alloys [J]. Surface and Coatings Technology, 2022, 431: 128000−128009.

[7] SHIMIZU T, IIKUBO T, ISOBE S. Cyclic oxidation resistance of an intermetallic compound TiAl [J]. Materials Science and Engineering: A, 1992, 153: 602−607.

[8] HU Yuan-tao, ZHENG Lei, YAN Hao-jie, WU Lian-kui, LIN Xiang-jun, CAO Fa-he, JIANG Mei-yuan. Improving hot corrosion resistance of aluminized TiAl alloy by anodization and pre-oxidation [J]. Transactions of Nonferrous Metals Society of China, 2021, 31: 193−206.

[9] LUO Yao-feng, LU Rui-yu, WANG Yan, LIU Bin, YANG Hai-tang, LIU Yong. Interfacial reaction in Al_2O_3 fiber reinforced TiAl matrix composite [J]. Transactions of Nonferrous Metals Society of China, 2023, 33: 2054−2063

[10] CHENG Yu-xian, WANG Wen, ZHU Sheng-long, XIN LI, WANG Fu-hui. Arc ion plated-Cr_2O_3 intermediate film as a diffusion barrier between NiCrAlY and γ-TiAl [J]. Intermetallics, 2010, 18: 736−739.

[11] HAN Di-juan, LIU Dong-dong, NIU Ya-ran, QI Zhi-xiang, PAN Yang-yang, XU Hao, ZHENG Xue-bin, CHEN Guang. Interface stability of NiCrAlY coating without and with a Cr or Mo diffusion barrier on Ti−42Al−5Mn alloy [J]. Corrosion Science, 2021, 188: 109538−109548.

[12] LUO Xian, LI Chao, YANG Yan-qing, XU Hai-man, LI Xiao-yu, LIU Shuai, LI Peng-tao. Microstructure and interface thermal stability of C/Mo double-coated SiC fiber reinforced γ-TiAl matrix composites [J]. Transactions of Nonferrous Metals Society of China, 2016, 26: 1317−1325.

[13] LAFONT M C, JUAREZ L F, VAHLAS C. Transmission electron microscopy of Re and Ru films deposited on NiCoCrAlYTa powders [J]. Scripta Materialia, 2004, 51: 699−703.

[14] PEREIRA J C, ZAMBRANO J C, AFONSO C R M, AMIGÓ V. Microstructure and mechanical properties of NiCoCrAlYTa alloy processed by press and sintering route [J]. Materials Characterization, 2015, 101: 159−165.

[15] JUÁREZ L F, VAHLAS C, ALVAREZ C J A. Microstructural characterization of Ru-doped NiCoCrAlYTa coupons treated by thermal oxidation [J]. Corrosion Science, 2009, 51: 2192−2196.

[16] ZHANG Ke-ren, HU Rui, LEI Tian-cheng, YANG Jie-ren. Refinement of massive γ phase with enhanced properties in a Ta containing γ-TiAl-based alloys [J]. Scripta Materialia, 2019, 172: 113−118.

[17] YUAN Cheng-hao, LIU Bin, LIU Yu-xi, LIU Yong. Processing map and hot deformation behavior of Ta-particle reinforced TiAl composite [J]. Transactions of Nonferrous Metals Society of China, 2020, 30: 657−667.

[18] HUANG Ji-bo, SUN Wen, CHU Xin, LAN Hai-ming, XIE Ying-chun, YE Dong-dong, HUANG Ren-zhong. Effect of high temperature exposure on microstructure, mechanical and tribological properties of cold sprayed NiCoCrAlTaY coatings [J]. Surface and Coatings Technology, 2023, 462: 129466−129476.

[19] CHEN Rui-run, GONG Xue, WANG You, QIN Gang, ZHANG Nan-nan, SU Yan-qing, DING Hong-sheng, GUO Jing-jie, FU Heng-zhi. Microstructure and oxidation behaviour of plasma-sprayed NiCoCrAlY coatings with and without Ta on Ti44Al6Nb1Cr alloys [J]. Corrosion Science, 2018, 136: 244−254.

[20] SUN Xiao-yu, ZHANG Pi-min, MOVERARE J, LI Xin-hai, CUI Lu-qing, PENG Ru-lin. Impeding the γ' depletion during the interdiffusion between bond coatings and superalloys via introduction of tantalum in bond coatings [J]. Materials & Design, 2023, 227: 111792−111804.

[21] XU Zhong, XIONG F F. Plasma surface metallurgy with double glow discharge technology [M], 1st ed. Beijing: Springer, 2017.

[22] ZAMANI P, VALEFI Z. Characterization and early-stage oxidation behavior of CoNiCrAlY/nano-Al_2O_3 composite coatings using satellited powders deposited by HVOF and LPPS processes [J]. Journal of Thermal Spray Technology, 2023, 32: 2525−2538.

[23] ZAMANI P, VALEFI Z. Comparative investigation of microstructure and high-temperature oxidation resistance of high-velocity oxy-fuel sprayed CoNiCrAlY/nano−Al_2O_3 composite coatings using satellited powders [J]. International Journal of Minerals, Metallurgy and Materials, 2023, 30: 1779−1791.

[24] ZAMANI P, VALEFI Z. Correlation between microstructure, phase composition and oxidation behavior of CoNiCrAlY/nano-Al_2O_3 coatings using satellited feedstock deposited by LPPS process [J]. Surface and Coatings Technology, 2023, 474: 130112−130128.

[25] LIU Xiao-ping, YOU Kai, WANG Zhen-xia, ZHANG Min-quan, HE Zhi-yong. Effect of Mo-alloyed layer on oxidation behavior of TiAl-based alloy [J]. Vacuum, 2013, 89: 209−214.

[26] ZHOU Bing, WANG Ya-rong, ZHENG Ke, MA Yong, WANG Yong-sheng, YU Sheng-wang, WU Yu-cheng. Anti-oxidation characteristics of Cr-coating on the surface of Ti−45Al−8.5Nb alloy by plasma surface metallurgy technique [J]. Chinese Physics B, 2020, 29: 126101−126110.

[27] ZHENG Ke, WANG Ya-rong, WANG Rui-ying, WANG Yan-li, CHENG Fang, MA Yong, HEI Hong-jun, GAO Jie, ZHOU Bing, WANG Yong-sheng, LIANG Yong-feng, YU Sheng-wang, TANG Bin, LIN Jun-pin, WU Yu-cheng. Microstructure, oxidation behavior and adhesion of a CoNiCrAlTaY coating deposited on a high Nb−TiAl alloy by plasma surface metallizing technique [J]. Vacuum, 2020, 179: 109494−109503.

[28] CUI Shi-yu, MIAO Qiang, LIANG Wen-ping, LI Bai-qiang. Oxidation behavior of NiCoCrAlY coatings deposited by double-Glow plasma alloying [J]. Applied Surface Science, 2018, 428: 781−787.

[29] QIU Zhong-kai, ZHANG Ping-ze, WEI Dong-bo, DUAN Bao-zhang, ZHOU Peng. Tribological behavior of CrCoNiAlTiY coating synthesized by double-glow plasma surface alloying technique [J]. Tribology International, 2015, 92: 512−518.

[30] CUI Shi-yu, YI Zhou, HUANG Jun, DONG Chao, LUO Jun-ming, QUYANG Jiang, TAO Xiao-ma. The preparation and lubrication properties of a CrN/Cr multilayer using the double glow plasma surface alloying technique [J]. Applied Surface Science, 2022, 605: 154686−154696.

[31] ANSARI M, SHOJA-RAZAVI R, BAREKAT M, MAN H C. High-temperature oxidation behavior of laser-aided additively manufactured NiCrAlY coating [J]. Corrosion Science, 2017, 118: 168−177.

[32] POLETAEV D O, LIPNITSKII A G, MAKSIMENKO V N, KOLOBOV Y R, BERESNEV A G, GUSAKOV M S. The N-body interatomic potentials for molecular dynamics simulations of diffusion in C15 Cr_2Ta Laves phase [J]. Computational Materials Science, 2023, 216: 111841−111851.

[33] TIEN R H, ZHU J H, LIU C T, WALKER L R. Effect of Ru additions on microstructure and mechanical properties of $Cr-TaCr_2$ alloys [J]. Intermetallics, 2005, 13: 361−366.

[34] DU Y, SCHMID-FETZER R. Thermodynamic modeling of the Al−Ta system [J]. Journal of Phase Equilibria, 1996, 17: 311−324.

[35] SUBRAMANIAN P R, MIRACLE D B, MAZDIYASNI S. Phase relationships in the Al−Ta system [J]. Metallurgical Transactions A, 1990, 21: 539−545.

[36] ZHANG Bang-yan, YANG Guang-jun, LI Cheng-xin, LI Chang-jiu. Non-parabolic isothermal oxidation kinetics of low pressure plasma sprayed MCrAlY bond coat [J]. Applied Surface Science, 2017, 406: 99−109.

[37] ELLINGHAM H J T. Reducibility of oxides and sulphides in metallurgical processes [J]. Journal of the Society of Chemical Industry, 1944, 63: 125−160.

[38] MOORE J J. Chemical Metallurgy [M]. 1st ed. London: Elsevier, 1981.

[39] KUMAR K S, PANG L X, LIU C T, HORTON J, KENIK E A. Structural stability of the Laves phase Cr_2Ta in a two-phase $Cr-Cr_2Ta$ alloy [J]. Acta Materialia, 2000, 48: 911−923.

[40] YAO Jing, LU Shi-qiang, XIAO Xuan, DENG Li-ping. Effect of molybdenum on the microstructure and oxidation behavior of hot-pressed $TaCr_2$ alloys [J]. Metal Science and Heat Treatment, 2019, 61: 249−255.

[41] BHOWMIK A, PANG Hon-tong, EDMONDS I M, RAE C M F, STONE H J. Effect of silicon additions on the high temperature oxidation behaviour of $Cr-Cr_2Ta$ alloys [J]. Intermetallics, 2013, 32: 373−383.

[42] DAROONPARVAR M, YAJID M A M, KAY C M, BAKHSHESHI-RAD H, GUPTA R K, YUSOF N M, GHANDVAR H, ARSHAD A, ZULKIFLI I S M. Effects of Al_2O_3 diffusion barrier layer (including Y-containing small oxide precipitates) and nanostructured YSZ top coat on the oxidation behavior of HVOF NiCoCrAlTaY/APS YSZ coatings at 1100 °C [J]. Corrosion Science, 2018, 144: 13−34.

[43] CHUNG C K, CHANG Y L, CHEN T S, SU P J. Annealing effects on microstructure and properties of Ta−Al thin film resistors [J]. Surface and Coatings Technology, 2006, 201: 4195−4200.

[44] KOFSTAD P, ESPEVIK S. Oxidation of tantalum coated with aluminum and aluminum-chromium alloys [J]. Journal of the Less Common Metals, 1967, 12: 117−138.

[45] MITSUI H, HABAZAKI H, HASHIMOTO K, MROWEC S. The sulfidation and oxidation behavior of sputter-deposited Al−Ta alloys at high temperatures [J]. Corrosion Science, 1997, 39: 59−76.

[46] TEIXEIRA V. Mechanical integrity in PVD coatings due to the presence of residual stresses [J]. Thin Solid Films, 2001, 392: 276−281.

[47] TEIXEIRA V. Residual stress and cracking in thin PVD coatings [J]. Vacuum, 2002, 64: 393−399.

[48] WANG Yi, FANG Hua-zhi, ZACHERL C L, MEI Zhi-gang, SHANG Shun-li, CHEN Long-qing, JABLONSKI P D, LIU Zi-kui. First-principles lattice dynamics, thermodynamics, and elasticity of Cr_2O_3 [J]. Surface Science, 2012, 606: 1422−1425.

[49] TEXIER D, MONCEAU D, HERVIER Z, ANDRIEU E. Effect of interdiffusion on mechanical and thermal expansion properties at high temperature of a MCrAlY coated Ni-based superalloy [J]. Surface and Coatings Technology, 2016, 307: 81−90.

[50] PAN Yang-yang, LIANG Bo, NIU Ya-ran, TIAN Jin, HAN Di-juan, ZHONG Xin, XIE Ling-ling, ZHENG Xue-bin. Thermal shock behaviors of plasma sprayed YSZ/TiAlCrY system on TiAl alloys [J]. Ceramics International, 2022, 48: 6199−6207.

[51] CHRISTENSEN R J, TOLPYGO V K, CLARKE D R. The influence of the reactive element yttrium on the stress in alumina scales formed by oxidation [J]. Acta Materialia, 1997, 45: 1761−1766.

[52] MA A-min, LIU Dao-xin, ZHANG Xiao-hua, LIU Yan-jie, ZHAO Wei-dong, WANG Ruo-lei, HE Guang-yu. Improving fatigue performance of TiZrN/TiZr-coated Ti−6Al−4V alloy by inducing a stabile compressive residual stress field [J]. Journal of Alloys and Compounds, 2022, 925: 166799−166808.

γ-TiAl 合金表面 Cr/CoNiCrAlTaY 双层抗氧化防护涂层的制备及界面表征

曾 臻[1]，王永胜[1]，王亚榕[1]，周 兵[1]，郑 可[1]，桂万元[2]，王艳丽[3]，于盛旺[1]，林均品[3]

1. 太原理工大学 材料科学与工程学院，太原 030024；
2. 北京科技大学 国家安全服役中心，北京 100083；
3. 北京科技大学 新金属材料国家重点实验室，北京 100083

摘　要：采用等离子体表面冶金技术在 Ti−45Al−8.5Nb 合金表面制备 Cr/CoNiCrAlTaY 双层涂层。涂层由最外层的 Cr 和 CoNiCrAlTaY 过渡层组成，晶粒尺寸约为 2 μm，具有致密的显微组织和良好的冶金结合力。在 1173 K 下氧化时，涂层质量增量与时间呈典型幂指数关系，速率指数为 3.18。合金表面形成了保护性膜如 Cr_2O_3 以及尖晶石氧化物如 $NiCr_2O_4$ 和 $CoCr_2O_4$，并且其氧化反应速率较低。界面分析发现，Ta 析出相(包括 Cr_2Ta 和 $TaAl_3$)以及 Ta 氧化物(如 Ta_2O_5 和 Ta_2O_3)对于延缓扩散、增强结合力和提高抗氧化性能起到重要作用。

关键词：TiAl 合金；Cr/CoNiCrAlTaY 涂层；抗氧化性；界面；附着力

(Edited by Xiang-qun LI)